N O T I C E

THIS DOCUMENT HAS BEEN REPRODUCED FROM MICROFICHE. ALTHOUGH IT IS RECOGNIZED THAT CERTAIN PORTIONS ARE ILLEGIBLE, IT IS BEING RELEASED IN THE INTEREST OF MAKING AVAILABLE AS MUCH INFORMATION AS POSSIBLE

NASA

Technical Memorandum TM 82157

On the Compensation of Geoid Anomalies Due to Subducting Slabs

David C. McAdoo

JUNE 1981

National Aeronautics and Space Administration

Goddard Space Flight Center
Greenbelt, Maryland 20771

"Page missing from available version"

ON THE COMPENSATION OF GEOID ANOMALIES DUE TO SUBDUCTING SLABS

ABSTRACT

Candidate models of the forces which oppose the sinking of slabs are all constrained to produce results consistent with the following observation: relative geoid highs, which one assumes are due to slabs, characteristically occur over subduction zones. Certain models which are otherwise plausible, such as those based on a Newtonian half-space mantle, yield geoid lows instead of highs. This study has extended a published model of viscous corner flow in subduction zones in order to demonstrate that it can – in certain cases – produce the requisite geoid highs. Specifically the relative geoid highs are produced if mantle flow is distinctly non-Newtonian (stress exponent $n > 2$). Results in the form of deflection of vertical (or geoid slope) profiles are computed for typical values of the slab parameters; they are compared with a representative profile of geoid slopes derived from Seasat altimeter data in order to show qualitative similarities. It is concluded that the effect of non-Newtonian flow as opposed to Newtonian, is to spread out the induced surface deformation, thereby stretching out the regional compensation to wavelengths, (transverse to the trench) of several thousand kilometers.

ON THE COMPENSATION OF GEOID ANOMALIES DUE TO SUBDUCTING SLABS

INTRODUCTION

It is generally accepted that the lithosphere warms rather sluggishly as it descends into the mantle. As the cool slab is hydrostatically compressed it becomes relatively dense. A number of workers (McKenzie, 1969; Griggs, 1972; Kaula, 1972) have suggested that gravity (geoidal) highs observed over subduction zones may be due to the dense sinking slab. Recent work confirms this relationship between geoid high and subducting slab. Global scale modelling by Chase (1979) and Crough and Jurdy (1980) does so. A regional study by McAdoo (1981a) which uses Geos-3 and Seasat altimeter data also supports such a relationship.

Griggs (1973) stated and McKenzie (1969) implied that positive gravity anomalies (or geoid anomalies) due to the slab must be regionally compensated. Griggs (1973) also pointed out that the negative anomaly associated with the actual trench serves to partially compensate the positive anomaly due to the slab. In fact this partial compensation due to the trench can be expected to be more pronounced in a geoid height representation than in a gravity anomaly characterization such as that used by Griggs. Trenches such as the Aleutian produce a short wavelength ($\lambda<400$ km, transverse to trench) negative gravity anomaly; however they produce a corresponding negative geoid anomaly which has significant short and long wavelength (long wavelengths comparable to slab anomaly) components. According to McAdoo [1981b] the negative anomaly due to the Aleutian trench is not sufficient to fully compensate the geoid anomaly due to the Aleutian slab. In fact this study suggests that complete regional compensation involves induced surface deformation with wavelengths transverse to the trench of several thousand kilometers.

It is perhaps surprising that the broad geoidal highs typically observed over subduction zones do exist at all. More specifically, certain models suggest that the stress field induced by the sinking slab will give rise to a surface deformation and a concomitant geoid low which completely compensates the geoid high due to the relatively dense slab. Morgan's (1965) model of a dense cylinder

sinking in a uniformly viscous mantle (Newtonian) produces, as a net result, a broad geoid low. Numerical experiments by McKenzie et al. (1980) on convection yielded geoid lows over the descending flow limbs. Cold and hot blobs were introduced to drive the time dependent flow. Davies' (1981) model of regional compensation of subducting slabs includes supporting stresses transmitted both up the slab and through the surrounding mantle. Just as the preceding models do, this model produces a net geoid low (see dashed line in Figure 4, Davies, 1981) for the case of complete compensation, i.e., the case in which the magnitude of the supporting forces equals that of the sinking forces

A corner flow model like the one used by Tovish et al. (1978), Stevenson and Turner (1977) or McKenzie (1969) represents the kinematics of subduction more exactly than does either the sinking cylinder model (Morgan, 1965) or the convection/blob model (McKenzie et al., 1980). Tovish et al. (1978) demonstrated that the induced flow in the mantle gives rise to dynamic pressures on the slab which may substantially counterbalance the gravitational torque on the slab. The gravitational torque alone would cause the slab to hang straight down. Upon assuming that the torque due to induced flow exactly counterbalances the gravitational torque one can compute a net geoid signal. This paper is primarily devoted to computing such a signal. The computations indicate that a geoid low should occur over the subduction zones if the flow is nearly Newtonian. This result is in agreement with those of the two models cited above. However the computations also suggest that if the flow is substantially non-Newtonian a relative geoid high occurs over the subducting slab. The computed geoid highs have approximately the same wavelength as those actually observed over subducting slabs.

THE CORNER FLOW MODEL

As the slab founders it induces stresses in the surrounding mantle. These induced stresses give rise to a deformation of the surface which will affect the gravity field. Tovish et al. (1978) have developed a corner flow model of this induced flow. Their model will be used in this study to generate the induced stress field. The model provides analytical solutions for the induced stress field in a Newtonian or non-Newtonian mantle. More specifically, the appropriate constitutive equation is given by

$$\dot{e} = \eta_n \tau^n \tag{1}$$

where $\dot{e}$ is strain rate, η_n is a proportionality constant, τ is stress and n is constant. By definition, n = 1 if the material behaviour is Newtonian. The model geometry and kinematics are shown in Figure 1. The slab is flat, its dip angle remains fixed, it is hinged (has infinite curvature) at its upper end, and subducts at a speed V_c. The mantle is assumed uniform in rheology (η_n, n are constant) throughout. Body forces internal to the mantle which result from temperature variations are neglected as are inertial forces.

Tovish et al. obtain a solution for the induced stress field, σ_{ij}, as follows.

$$\sigma_{ij} = \begin{bmatrix} p & \tau_{r\theta} \\ \tau_{r\theta} & p \end{bmatrix} \tag{2}$$

where dynamic pressures p are given by

$$p(r, \theta) = \pi_o (2\eta_n r)^{-1/n} \sin\left((2n-1)^{1/2} (\theta + \theta_o)/n\right) \tag{3}$$

and shear stresses by

$$\tau_{r\theta}(r, \theta) = \pi_o \frac{(2\eta_n r)^{-1/n}}{(2n-1)^{1/2}} \cos\left((2n-1)^{1/2} (\theta + \theta_o)/n\right). \tag{4}$$

Constants π_o and θ_o are obtained by applying the appropriate boundary conditions (see Figure 1) to the velocity solution. Values of π_o and θ_o are listed in Table I for different values of stress exponent, n. Actually these constants plus two others, Θ_0 and Θ_1, are necessary to completely specify the velocity field as given in Tovish et al. (1978). For completeness all four constants are shown in Table I. The constants are computed for n = 1, 2, 3, 5 and a slab dip angle of $\alpha = 60°$. They are obtained from four coupled nonlinear algebraic equations (excluding n = 1), and are solved numerically. Note that Tovish et al. also computed constants for n = 1, 3 some of which are in error (G. Schubert, personal communication) and therefore do not agree with values in Table 1. Note also that certain of their equations (specifically A-10, A-12, A-20 and A-21) contain minor typographical errors. The imaginary constants in Table 1 for the n = 2 case are easily understood if one recalls that constant η_n in (1) becomes negative when shear stress, τ,

Table I

Values of Constants in Corner Flow Stress and Velocity Field Expressions (dip $\alpha = 60°$)
See text for explanations.

	n = 1		n = 2		n = 3		n = 5	
Coupled Boundary Conditions								
	ocean	arc	ocean	arc*	ocean	arc	ocean	arc
$\pi_o/V_c^{1/n}$	-0.676	-5.594	2.964i	-7.172*	-2.015	+9.101	-2.825	-13.062
Θ_0/V_c	+0.707	+3.164	+2.231	-8.044*	+1.574	-75.385	+1.078	-1035.22
Θ_1/V_c	0.0	0.0	+1.288	-9.948*	+0.909	+56.761	+0.622	+741.46
θ_o	-60.024°	+50.688°	+43.923°	+66.005°	-60.0°	-157.692°	-60.0°	+114.390°
	*Valid only when $\theta > 37.93°$ (i.e. $\tau_{r\theta} > 0$); for $\theta < 37.93°$: $\pi_o V_c^{-1/n} = -7.172i$, $\Theta_0/V_c = +7.765$, $\Theta_1/V_c = +10.338$							
Decoupled Boundary Conditions								
	n = 1		n = 2		n = 3		n = 5	
	ocean	arc	ocean	arc	ocean	arc	ocean	arc
$\pi_o/V_c^{1/n}$	-0.685	-2.282	1.562i	3.955i	-2.278	-5.088	-3.530	-7.283
Θ_0/V_c	+0.829	+1.705	+0.836	+3.192	+0.991	-8.381	+1.103	-34.391
Θ_1/V_c	0.0	0.0	+0.227	+2.294	+1.717	+14.518	+1.910	+59.567
θ_o	-30.0°	+30.0°	-16.077°	+43.923°	+0.748°	+60.748°	+30.0°	+90.0°

is negative. When η_n is negative and n = 2, the term $(2\eta_n r)^{-1/n}$ in (3) and (4) becomes imaginary. For the case in which n = 2 and boundary conditions are coupled, the arc regime has a sector of positive shear stress and one of negative shear stress; therefore a piecewise solution of the constants is required.

SLOPE OF THE GEOID: ANALYTICAL EXPRESSIONS

The corner flow model above does not include any stress or deformation conditions along the lower boundary of the unsubducted lithosphere. In fact it will be assumed (as in McKenzie, 1969) that the lower surface (and upper surface) of the lithosphere deform such that the impinging normal stress vanishes. In other words the pressure equations, (2) and (3), determine the deformation of the lithosphere. The strength of the lithosphere will be ignored as the horizontal extent of the induced pressure field is substantially greater than the characteristic wavelength (~300 km) of the lithosphere's response to transverse loads. Therefore the induced pressure p'(x) along the lower surface of the lithosphere causes a deformation, h(x), given by

$$h(x) = p'(x, z = 0)/\rho g \tag{5}$$

where ρ is an average density for the lithosphere/upper mantle, g is the acceleration of gravity, h is positive upwards, p is positive in compression and x is defined in Figure 2. The gravitational effect of this deformation can be obtained by introducing an equivalent surface mass layer of mass per unit area,

$$\sigma_p(x) = \frac{p'(x, z = 0)}{g} . \tag{6}$$

The solution for induced pressure, p, as shown in (3) above may be substituted in (6) by using the following change of variables

$$p'(x, 0) = \begin{cases} p(r = x, \theta = \alpha), & x > 0 \\ p(r = -x, \theta = \pi - \alpha), & x < 0 . \end{cases} \tag{7}$$

It is assumed implicitly in equation (7) that slab thickness is effectively zero (cf. Figure 2). Note that for all cases covered in Table 1 pressure p'(x, 0) is everywhere negative (tensile) as is $\sigma_p(x, 0)$.

The gravitational effect of the induced surface deformation in (5) or (6) can be obtained by evaluating the following integral expression for the slope of the geoid (or deflection of the vertical)

$$\frac{dN}{dx}(x, z=-d) = \frac{-2G}{g}\int_{-\infty}^{\infty} \frac{\sigma_p(\xi)\cdot(x-\xi)}{(x-\xi)^2+d^2}\,d\xi \tag{8}$$

where G is the universal gravitational constant, g is the acceleration of gravity and d is the separation distance between sea level and uppermost lithosphere as shown in Figure 2. It should be recalled that the corner flow model is two-dimensional (x, z) and extends to infinity in directions normal to the x, z plane. Therefore the surface mass layer σ_p exists everywhere on the z = 0 plane and integrals having the form of (8) in many cases can not be evaluated (diverge). By successive substitution of (3) into (7), then (7) into (6), and (6) into (8) one obtains a convergent integral for slope of the geoid (when n > 1). Upon evaluating the integral in (8) using equation 3.252.12 in Gradsteyn and Ryzhik (1980) one obtains the expression for slope as follows:

$$\frac{dN}{dx}(x, z=-d) = -2\pi G\tilde{g}^2 d^{-1}(x^2+d^2)^{-\frac{1}{2}n}\left\{ x\,\mathrm{cosec}\,(\pi(1-1/n))\cdot\left[C_1\sin\frac{t_1}{n} + C_2\sin\frac{t_2}{n}\right] + (x^2+d^2)^{\frac{1}{2}}\,\mathrm{cosec}\,(\pi(2-1/n))\cdot\left[C_1\sin\left(\left(1-\frac{1}{n}\right)t_1\right) - C_2\sin\left(\left(1-\frac{1}{n}\right)t_2\right)\right]\right\} \tag{9}$$

where $t_1 = \arccos\left\{\frac{-x}{(x^2+d^2)^{\frac{1}{2}}}\right\}$, $t_2 = \arccos\left\{\frac{+x}{(x^2+d^2)^{\frac{1}{2}}}\right\}$

and where $C_1 = \pi_{oa}(2\eta_n)^{-1/n}\sin\left((2n-1)^{\frac{1}{2}}(\alpha+\theta_{oa})/n\right)$,

$C_2 = \pi_{oo}(2\eta_n)^{-1/n}\sin\left((2n-1)^{\frac{1}{2}}(\pi-\alpha+\theta_{oo})/n\right)$.

Note that π_{oa}, θ_{oa} and π_{oo}, θ_{oo} are the values of constants π_o, θ_o in the expression for pressure (3) which apply in the case of the arc corner and oceanic corner respectively.

The corresponding integral necessary for obtaining the geoid itself can not be evaluated. (i.e., it blows up). Similarly the integral in (8) diverges if d = 0.

The expression (9), for geoid slope (deflection of the vertical) is evaluated and plotted in Figures 3 and 4 for dip angle $\alpha = 60°$ and stress exponents n = 2, 3, 5. For the Newtonian case, n = 1, the integral in (8) diverges and slopes can not be evaluated. Figure 3 represents the case of decoupled boundary conditions and Figure 4 represents the case of coupled boundary conditions.

All curves in Figures 3 and 4 can be interpreted as broad (wavelengths on the order of 10^3 km) geoidal lows. When represented as slopes (deflections of vertical) a geoid low characteristically has the approximate shape of an inverted "N" which has been streched horizontally and tilted counter-clockwise. This inverted "N" is, for example, evident in the n=2 curve of Figure 3. The curves in both Figures 3 and 4 have a gap between x=-250km and x= +250km. In fact, expression (9) yields a continuous curve (the reader may connect the halves in his mind's eye); however, the curves oscillate rather dramatically in this region (as do observed slopes; cf. Figure 8). Furthermore the model is unrealistic in this region due to the singularity in pressure, p(r = 0), and the assumption of an ignorable mechanical lithosphere. Values of the material constant η_n and subduction rate, V_c, are not specified to obtain the curves in Figures 3 and 4. Instead the ratio V_c/η_n is determined by postulating that torques on the slab due to induced pressure and gravity are in moment equilibrium. A uniform anomalous mass per unit area, σ_s, is specified for the slab as shown in Figure 2 and substituted into the moment equilibrium equation,

$$\frac{1}{2}\,\sigma_s g r_o^2 \cos\alpha + \int_0^{r_o} r p_a\,(r, 0)\,dr - \int_0^{r_o} r p_o\,(r, 0)\,dr = 0 \qquad (10)$$

where $p_a(r, 0)$ and $p_o(r, 0)$ are pressures given by equation (3) on the arc side and oceanic side, respectively, of the slab. In formulating (10) it is assumed that the thickness of the slab is effectively zero. By substituting (3) into (10) and rearranging one obtains the result,

$$\left(\frac{V_c}{2\eta_n d}\right)^{1/n} = \frac{(2-1/n)}{2}\,\sigma_s g\left(\frac{r_o}{d}\right)^{1/n}\cos\alpha\left[\frac{\pi_{oo}}{V_c^{1/n}}\sin\left((2n-1)^{1/2}\,\theta_{oo}/n\right)\right.$$

$$\left. - \frac{\pi_{oa}}{V_c^{1/n}}\sin\left((2n-1)^{1/2}\,\theta_{oa}/n\right)\right]^{-1} \qquad (11)$$

Upon assuming that $r_o = 550\ \text{km}/\sin 60^\circ$ and that $\sigma_s = 3 \times 10^5$ gm cm^{-2} which is reasonably consistent with thermal model predictions (cf. McAdoo, 1981a, b, Schubert et al., 1975), the following values are obtained for the sample case, n = 3 with decoupled boundary conditions:

$$\left(\frac{V_c}{2\eta_n d}\right)^{1/n} = 1.62 \times 10^8 \text{ dyne cm}^{-2} \qquad (12)$$

where d = 6 km;

$$\mu_e \cong 0.6 \times 10^{22} \text{ poises} \qquad (13)$$

where μ_e is effective viscosity defined as $\mu_e = (\tau^{1-n}/2\eta_n)$ and where τ and V_c are taken to be 5×10^7 dyne cm^{-2} and 5 cm/yr respectively. This viscosity is compared with those of other studies (e.g. Sleep, 1978) below. The quantity $(V_c/2\eta_n d)^{1/n}$ is needed to evaluate expression (9); it may be interpreted as a characteristic induced pressure.

Results in Figures 3 and 4 (also 6 and 7 below) are based on the assumed slab density $\sigma_s = 3.0 \times 10^5$ gm cm^{-2}; however, results for any value of σ_s may be readily obtained by a simple change in vertical scaling because dN/dx, given in (9), is proportional to σ_s.

Of course the geoid slopes given by (9) and displayed in Figures 3 and 4 do not include the effect of the anomalously dense slab itself. One can obtain the geoid slopes (deflections of vertical) due to the slab alone by evaluating the following expression

$$\frac{dN}{dx}(x) = -\frac{G\sigma_s}{g}\left\{-c\ln R^2 + 2\,\frac{(r-xc)(x-rc)}{R^2}\right.$$

$$\left. + 2\,\mathrm{sgn}(x)\,s\arctan\left(\frac{r-xc}{|xs|}\right) + 2\,|xs|\left(\frac{x^2s^2}{R^2}\right)\left(\frac{-c}{|xs|}\,\frac{-\mathrm{sgn}(x)(r-xc)}{x^2s}\right)\right\}\Bigg]_{\delta r}^{r_o+\delta r} \qquad (14)$$

where $$\mathrm{sgn}(x) \equiv \begin{cases} +1, & x \geq 0 \\ -1, & x < 0 \end{cases},$$

$$c \equiv \cos\alpha, \quad s \equiv \sin\alpha,$$

and $$R^2 \equiv x^2 + r^2 - 2xr\cos\alpha.$$

In the derivation of (14) the slab thickness is assumed to be negligible. The expression (14) is evaluated between limits $r_o + \delta r$ and δr which are (cf. Figure 2) the distance from slab's lower terminus to the trench and the distance from the slab's upper end to the trench. Expression (14) is easily derived from equation (15) in Chapman (1979) by using a co-ordinate transformation and a derivative operation. Figure 5 shows an evaluated result from (14) using the same parameter values that were employed in Figures 3 and 4, i.e. $\alpha = 60°$, $\sigma_o = 3 \times 10^5$ gm cm^{-2}, $r_o = (550/\sin 60°)$ km, $\delta r = (50/\sin 60°)$ km. The curve in Figure 5 has the shape of stretched, upright, clockwise-tilted "N," and therefore is representative of a relative geoid high.

The composite of both effects, that of the slab and that of induced surface deformation may be obtained by adding the results of Figure 5 to those of Figures 3 and 4 respectively. These summations are shown in Figures 6 and 7. As in Figures 3 and 4 the results between x = -250 km and x =+250km are omitted for reasons discussed above; once again, the viewer may wish to connect the matching curve halves in his mind's eye. For the nearly Newtonian cases (n = 2) one sees either the equivalent of geoid low (stretched, inverted 'N' shape) in the decoupled case (Figure 6) or a relatively flat signal in the coupled case (Figure 7); this indicates complete

compensation. However for the n = 3 and n = 5 cases, particularly those with coupled boundary conditions (Figure 7), the results are equivalent to a geoid high (i.e., they possess the characteristic stretched upright "N" shape).

OBSERVATIONS AND DISCUSSIONS

Geoid slope profiles obtained from model calculations can be compared with profiles of observed slopes. In general these observed profiles will be qualitatively similar to those model results based on assumed stress exponents $n \geq 3$ (strongly non-Newtonian). Figure 8 shows an observed sea surface slope profile derived from a pass of Seasat altimeter data over the eastern Aleutian arc. The corresponding sea surface height profile is also included in Figure 8. Ocean dynamics have not been removed with the exception of results from a global ocean tide model. However, most of the long-wavelength (>500 km) content of the sea surface slope signal in Figure 8 is geoid slope. The slope profile was derived using a running, least square estimate of slope over four-second (5 point/27 km) intervals. Ignoring the short-wavelength excursions in the observed slope curve of (Figure 8) one can see a stretched 'N' shape having the same sense, and roughly the same magnitude and wavelength as does, for example, the n = 3 model result in Figure 7. Large differences between absolute or average values of the model results (Figure 7; e.g, n = 5) and observed values (Figure 8) are to be expected. The rather arbitrary choice of reference ellipsoid. mean versus hydrostatic, may strongly affect the average observed slope. Furthermore, the average value of model results is distinctly negative (e.g, n = 5). which is largely due to a model artifacts, i.e., infinite extent in x plus rectilinearity.

Recall that the model calculations assumed that the slab dipped at an angle of 60°, extended to 600 km depth and possessed a density of $\sigma_0 = 3 \times 10^5$ gm/cm^2. A dip angle of 60° is not inconsistent with seismicity observations (see Jacob, 1972; Davies and House, 1979) for the Aleutian region covered by Seasat rev 553 in Figure 8; nor is the density estimate σ_0, inconsistent with inferred values (see McAdoo, 1981b; Grow, 1973) for this region. On the other hand, the slab model's maximum depth of 600 km substantially exceeds estimates (see Jacob, 1972; Davies and

House, 1979) of the maximum depth for the Benioff zone in this region. It has however been suggested by McAdoo (1981b) that the anomalously dense slab may extend to greater depths than the seismically inferred 250 km. The implicit viscosity ($\mu_e \sim 0.6 \times 10^{22}$ P, see above) is consistent with values used by Sleep (1978). In any case, theoretical and observational results show qualitative similarities; nothing more than this should be expected.

On progressively longer spatial scales (e.g., those of order one earth radius) this infinite plane model provides an increasingly poor representation of the actual geometry and process involved. Therefore a model based on spherical geometry is likely necessary to improve on the qualitative fits presented above.

Examination of model outputs in Figures 6 and 7 reveals that large geoid lows flank the subduction zone on the behind-arc side; somewhat smaller lows flank on the ocean side. It is tempting to speculate that two major lows in the global geoid may in part be due to subduction-induced surface deformation. The first low extends from central Asia through India and the eastern Indian ocean (see Figure 2 or 3, Lerch et al., 1979), and generally lies a few thousand kilometers behind major island arcs of the western Pacific. The second geoid low extends from the vicinity of the Bahamas southeastward across the general area of eastern Brazil, and lies behind the Middle American and South American arc.

CONCLUSION

The exact mechanism by which anomalously dense subducting slabs are supported has not been determined. However, candidate mechanisms must somehow preserve the characteristic relative geoid high which presumably results from the slab. Certain models based on a Newtonian half-space produce an induced surface deformation and concomitant geoid signals which completely compensate or wash out the relative geoid high due to the sinking slab. Tovish et al. (1978) presented a corner flow model which indicates that induced pressures may play a significant role in supporting the slab. This study extends their model and demonstrates that characteristic geoid highs are preserved if induced flow is the primary slab support mechanism and if the mantle is quite

non-Newtonia.. (stress exponent $n > 2$). Non-Newtonian flow effectively spreads out the induced surface deformation, thereby retaining relative geoid highs and forcing part of the regional compensation process out to long wavelengths. The capability of the induced flow mechanism to yield a net geoid high strongly suggests that it is a primary operative process at subduction zones.

ACKNOWLEDGMENTS

I would like to thank D. L. Turcotte for introducing me to corner flow problems. I am also grateful to G. H. Wyatt for providing and servicing a helpful computer program. G. F. Davies kindly provided a preprint of his paper.

REFERENCES

Chapman, M. E., Techniques for interpretation of geoid anomalies, *J. Geophys. Res.*, *84*, 3793-3801, 1979.

Chase, C. G., Subduction, the geoid, and lower mantle convection, *Nature*, *282*, 464-468, 1979.

Crough, S. T. and D. M. Jurdy, Subducted lithosphere, hotspots, and the geoid, *Earth Planet. Sci. Lett.*, *48*, 15-22, 1980.

Davies, G. F., Regional compensation of subducted lithosphere: effects on geoid, gravity, and topography from a preliminary model, *Earth Planet. Sci. Lett.*, in press, 1981.

Davies, J. N. and L. House, Aleutian subduction zone seismicity, volcano-trench spearation and their relation to great thrust-type earthquakes, *J. Geophys. Res.*, *84*, 4583-4591, 1979.

Gradsteyn, I. S. and M. Ryzhik, *Tables of Integrals Series and Products*, Translated by A. Jeffrey, 1980.

Griggs, D. T., The sinking lithosphere and the focal mechanisms of deep earthquakes, in *The Nature of the Solid Earth*, E. C. Robertson (editor), McGraw-Hill, New York, 361-384, 1972.

Grow, J. A., Coastal and upper mantle structure beneath the central Aleutian arc, *Bull Seism. Soc. Amer.*, *63*, 2155-2166, 1973.

Jacob, K., Global tectonic implications of anomalous seismic P travel times from the nuclear explosion Longshot, *J. Geophys. Res.*, *77*, 2556-2593, 1972.

Kaula, W. M., Global gravity and tectonics, *The nature of the solid earth*, E. C. Robertson (editor), 385-405, McGraw-Hill, New York, 1972.

Lerch, F. J., S. M. Klosko, R. E. Laubscher and C. A. Wagner, Gravity model improvement using Geos-3 (GEM-9 and -10), *J. Geophys. Res.*, *84*, 3897-3916, 1974.

McAdoo, D. C., Geoid anomalies in the vicinity of subduction zones, *J. Geophys. Res.*, in press, 1981a.

McAdoo, D. C., Geoid anomalies over the Alaskan/Aleutian subduction zone, *EOS Trans. AGU*, *62*, 389, 1981b.

McKenzie, D. P., Speculations on the consequences and causes of plate motions, *Geophys. J. R. Astr. Soc.*, *18*, 1-32, 1969.

McKenzie, D. P., A. Watts, B. Parsons and M. Roufosse, Plan form of mantle convection beneath the Pacific ocean, *Nature, 288,* 442-446, 1980.

Morgan, W. J. Gravity anomalies and convection currents, 1. & 2., *J. Geophys. Res., 70,* 6175-6204, 1965.

Schubert, G., D. A. Yuen and D. L. Turcotte, Role of phase transitions in a dynamic mantle, *Geophys J R Astr Soc., 42,* 705-735, 1975.

Sleep, N. H., The double seismic zone in downgoing slabs and the viscosity of the mesosphere, *J. Geophys. Res., 84,* 4565-4571, 1979.

Stevenson, D. J. and J. S. Turner, Angle of subduction, *Nature,* 334-336, 1977.

Tovish, A., G. Schubert and B. P. Luyendyk, Mantle flow pressure and the angle of subduction: non-Newtonian corner flows, *J. Geophys. Res., 83,* 5892-5898, 1978.

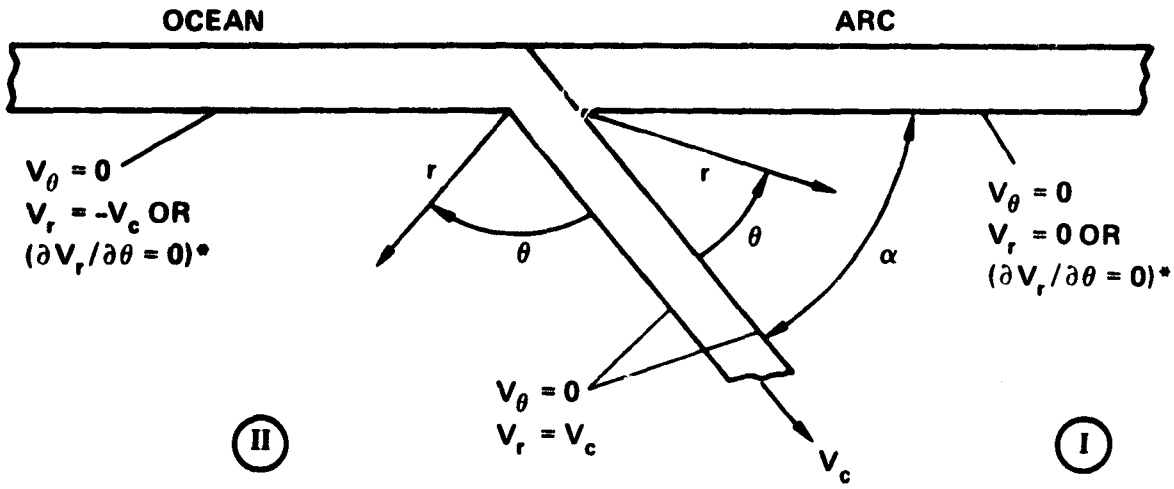

Figure 1. Geometry, plate kinematics and boundary conditions for the corner flow model due to Tovish et al. (1978). Two cases are shown: coupled and decoupled* boundary condition.

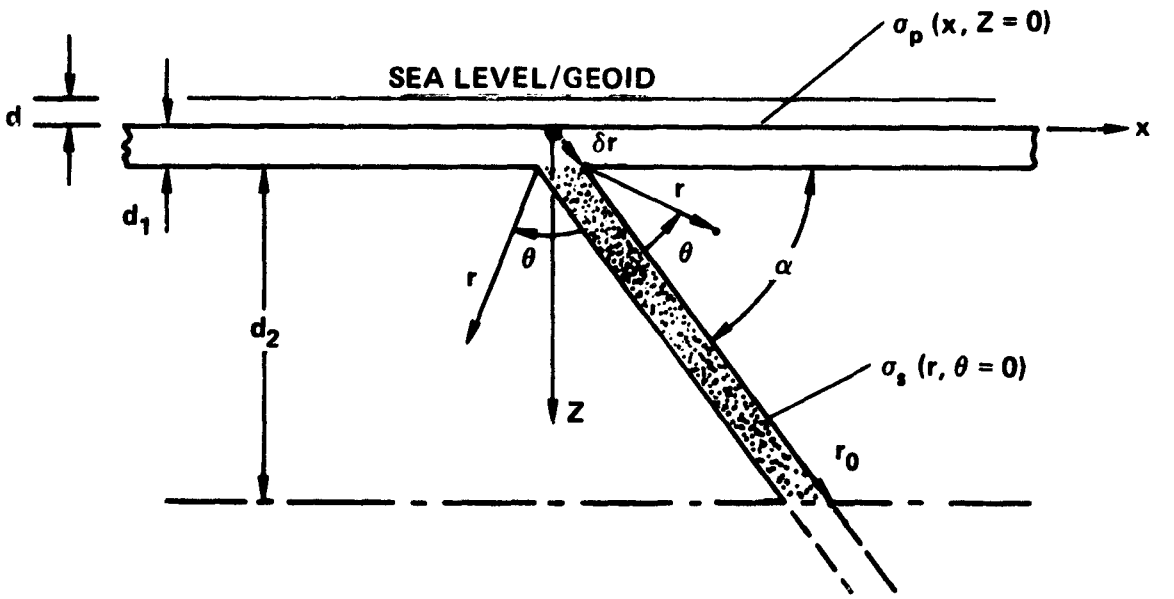

Figure 2. Geometry of the corner flow density model.

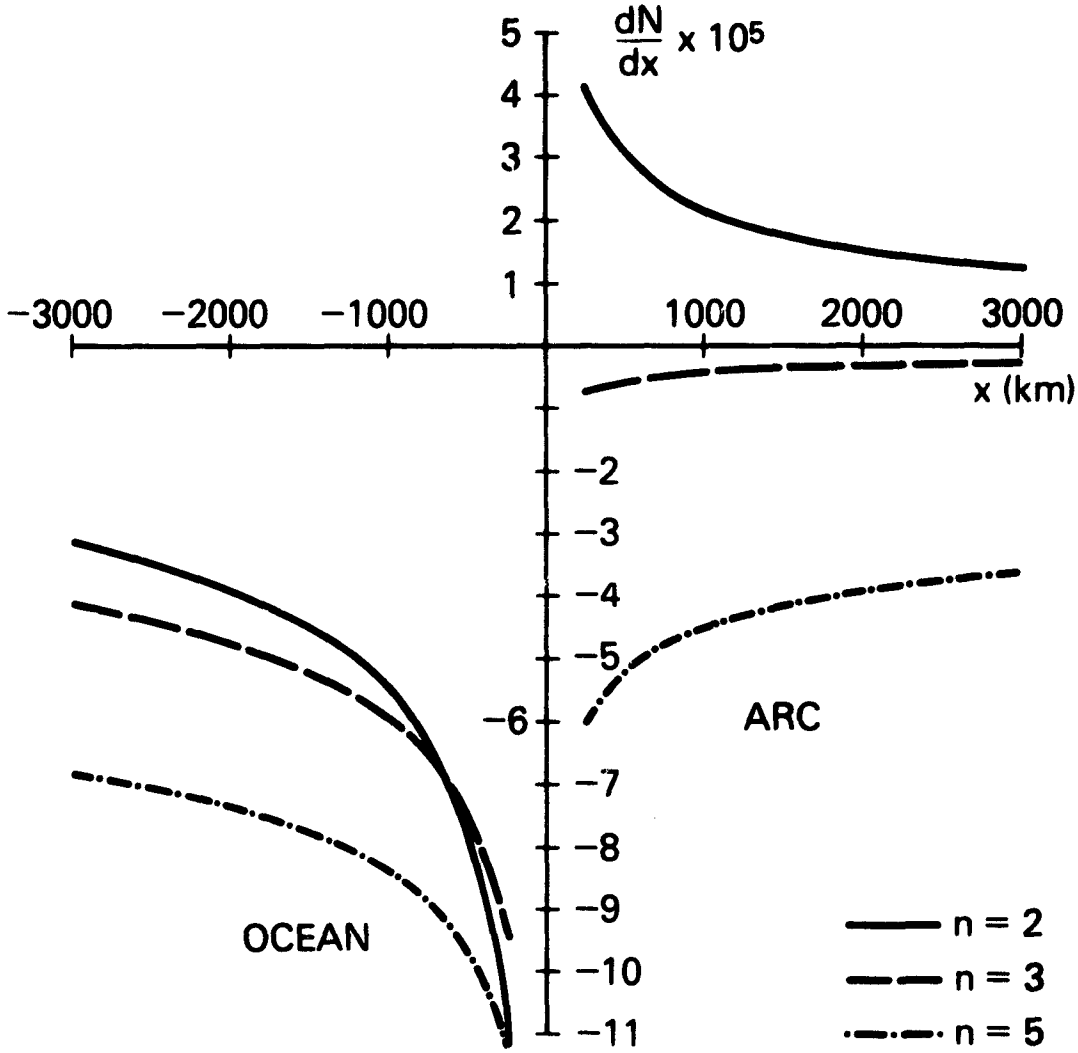

Figure 3. Geoid slope (or deflection of the vertical) versus transverse distance due to model of induced flow (alone). Decoupled boundary conditions are assumed. Three flow law cases (n= 2,3,5) included.

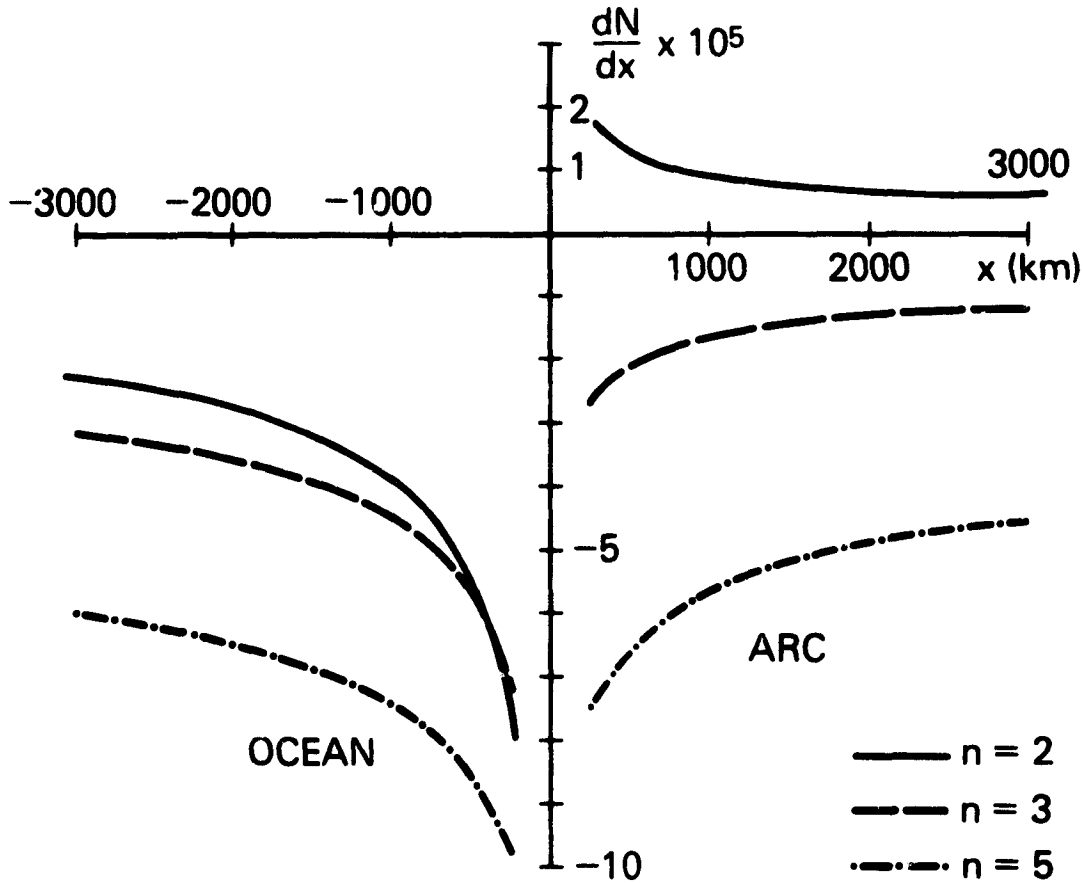

Figure 4. Geoid slope versus distance due to induced flow alone. Coupled boundary conditions are assumed. Three flow law cases included.

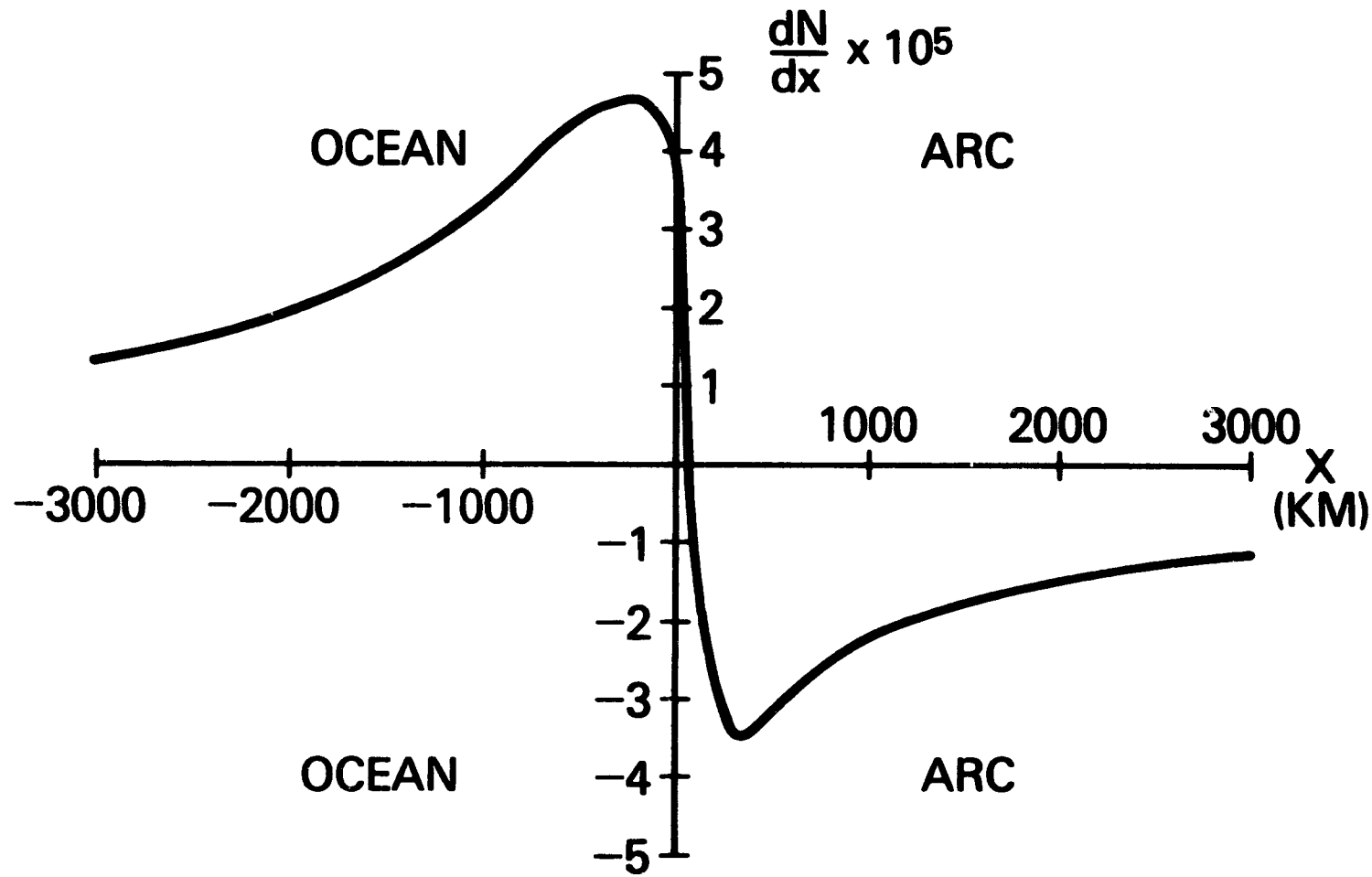

Figure 5. Geoid slope (or deflection of vertical) versus distance due to anomalously dense slab alone.

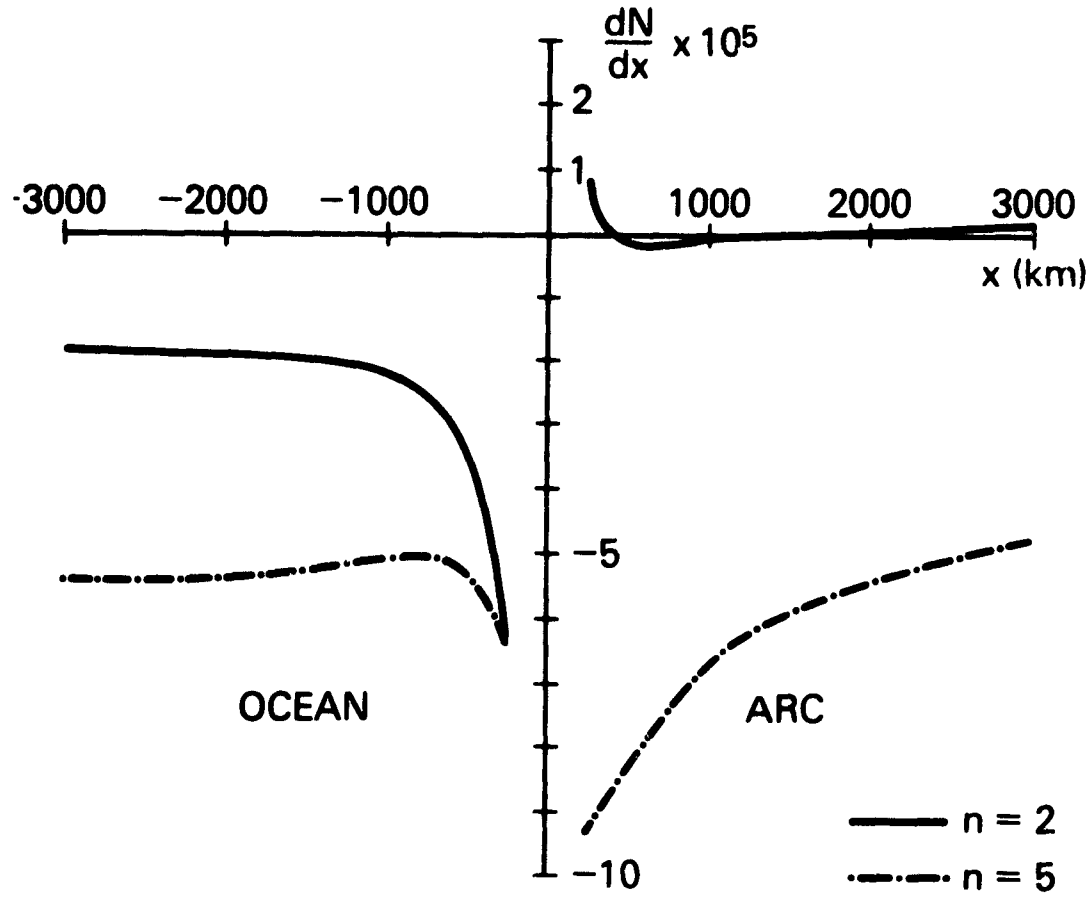

Figure 6. Geoid slope versus distance due to composite effect of induced flow (Figure 3) and slab (Figure 5). Decoupled boundary conditions assumed.

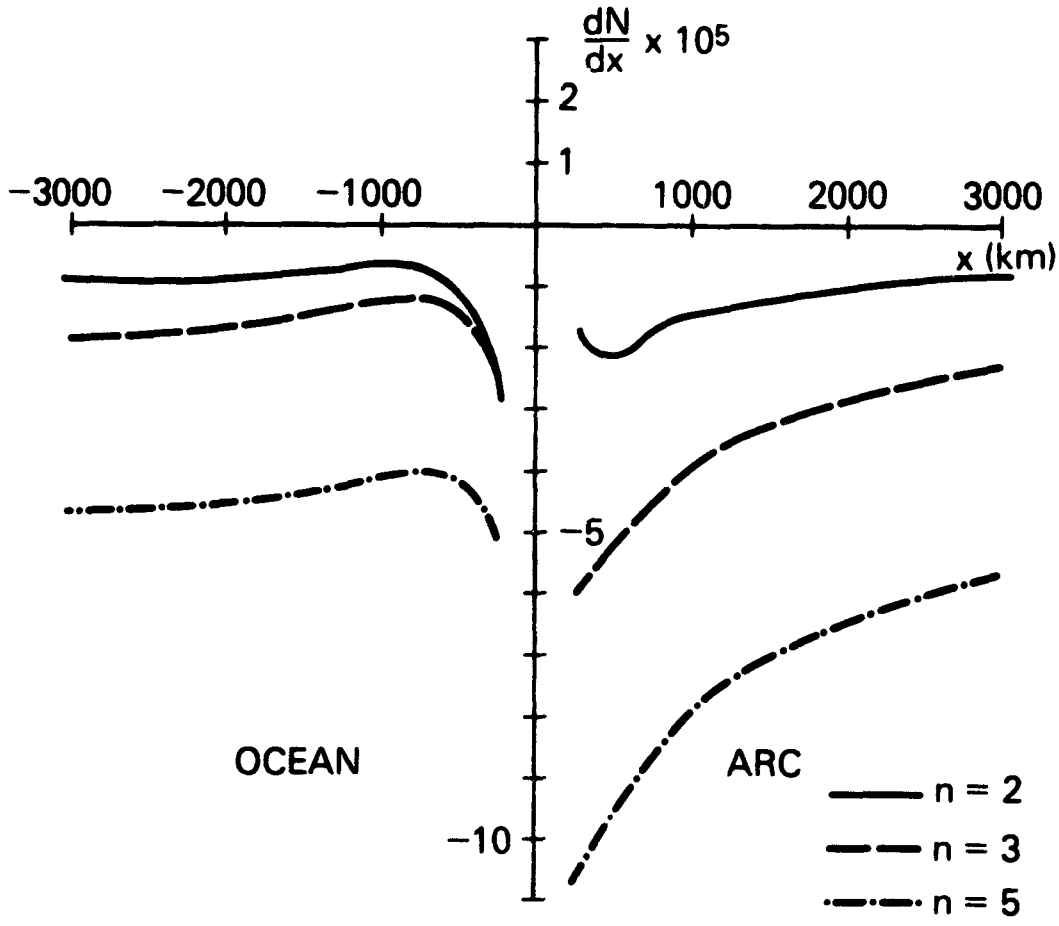

Figure 7. Geoid slope versus distance due to composite effect of induced flow (Figure 4) and slab (Figure 5). Coupled boundary conditions assumed.

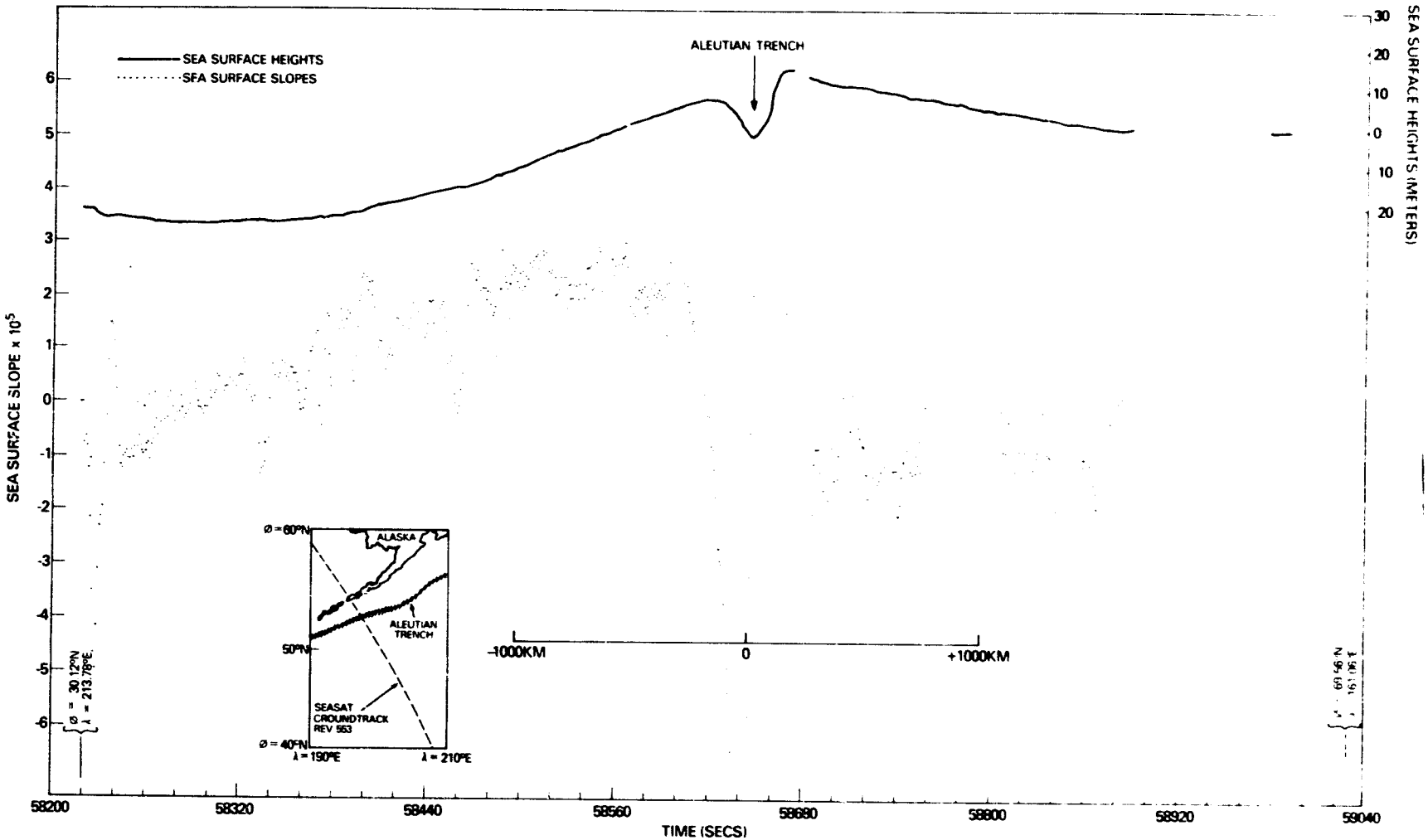

Figure 8. Profiles of sea surface heights and slopes of heights from Seasat altimeter rev 553. Reference ellipsoid with flattening 1/298.257 is used. Slopes obtained using a running, least squares technique.